energies

MDPI

Article

Non-Embedded Ultrasonic Detection for Pressure Cores of Natural Methane Hydrate-Bearing Sediments

Xingbo Li [1,†], Yu Liu [1,†], Hanquan Zhang [2], Bo Xiao [2], Xin Lv [3], Haiyuan Yao [3], Weixin Pang [3], Qingping Li [3], Lei Yang [1], Yongchen Song [1] and Jiafei Zhao [1,*]

1 Key Laboratory of Ocean Energy Utilization and Energy Conservation of Ministry of Education, Dalian University of Technology, Dalian 116024, China; Lixb1988@mail.dlut.edu.cn (X.L.); liuyu@dlut.edu.cn (Y.L.); leiyang@dlut.edu.cn (L.Y.); songyc@dlut.edu.cn (Y.S.)

2 Guangzhou Marine Geological Survey, Guangzhou 510075, China; 451379719@163.com (H.Z.); aggbf6056@163.com (B.X.)

3 Research Institute of China National Offshore Oil Corporation, Beijing 100027, China; lvxin@cnoon.com.cn (X.L.); yaohy2@cnoon.com.cn (H.Y.); pangwx@cnoon.com.cn (W.P.); liqp@cnoon.com.cn (Q.L.)

* Correspondence: jfzhao@dlut.edu.cn; Tel.: +86-159-4119-7989

† These authors contribute equally to this paper.

Received: 2 April 2019; Accepted: 22 May 2019; Published: 24 May 2019



Abstract: An apparatus for the analysis of pressure cores containing gas hydrates at in situ pressures was designed, and a series of experiments to determine the compressional wave response of hydrate-bearing sands were performed systematically in the laboratory. Considering the difficulties encountered in performing valid laboratory tests and in recovering intact hydrate bearing sediment samples, the laboratory approach enabled closer study than the marine environment due to sample recovery problems. The apparatus was designed to achieve in situ hydrate formation in bearing sediments and synchronous ultrasonic detection. The P-wave velocity measurements enabled quick and successive ultrasonic analysis of pressure cores. The factors influencing P-wave velocity (V_p), including hydrate saturation and formation methodology, were investigated. By controlling the initial water saturation and gas pressure, we conducted separate experiments for different hydrate saturation values ranging from 2% to 60%. The measured P-wave velocity varied from less than 1700 m/s to more than 3100 m/s in this saturation range. The hydrate saturation can be successfully predicted by a linear fitting of the attenuation (Q^{-1}) to the hydrate saturation. This approach provided a new method for acoustic measurement of the hydrate saturation when the arrival time of the first wave cannot be directly distinguished. Our results demonstrated that the specially designed non-embedded ultrasonic detection apparatus could determine the hydrate saturation and occurrence patterns in pressure cores, which could assist further hydrate resource exploration and detailed core analyses.

Keywords: non-embedded; pressure core; P-wave detection; hydrate saturation

1. Introduction

Natural gas hydrate has become a potential alternative energy source with the characteristics of being clean and having large reserves [1–3]. At present, the exploration and development of natural gas hydrates in various countries in the world have promoted considerable research and numerous techniques [4–7]. With the development of natural gas hydrate sampling techniques, the detection and analysis of gas hydrate pressure cores become the bridge that connects hydrate exploration and exploitation [8–10]. Natural gas hydrate pressure cores reflect the reservoir characteristics and hydrate

accumulation [11–13]. This information is important for the study of hydrate exploitation. The total amount of methane captured in the form of hydrate in nature is estimated to be on the order of $20{,}000 \times 10^{12}$ m^3. Their exploration and exploitation require a quick and effective analysis under in situ conditions.

To quantify seafloor methane hydrates over broad areas, remote geophysical methods are used to exploit the hydrate in sediment pores. Acoustic velocity is an important geophysical parameter from which we can know the lithology and saturation of the hydrate-bearing sediments [14]. The acoustic velocity measured in lab have already been used to assess the distribution and saturation of gas hydrates [15–18]. Waite [19] applied piezoelectric ceramic technology to hydrate-bearing sediment under high pressures. The effects of hydrate saturation on P-wave velocity were studied, the experimental results showed that P-wave velocity increased with the hydrate saturation. Yun [20] used acoustic technology for sand-tetrahydrofuran (THF) hydrate core acoustic measurement. The experimental results showed that THF hydrate mainly formed inside the pore when hydrate saturation was below 40%. Lee et al. [21] measured the THF hydrate cores of different porous media with acoustic measurements, and found that clay and glass sand had different effects on hydrate formation by the acoustic characteristics. Waite et al. [22] used a rock physics model to differentiate between potential pore-space hydrate distributions based on hydrate concentrations and P-wave velocity. The results of the model showed methane hydrate cemented unconsolidated sediment when forming in systems containing an abundant gas phase. However, quite a few field tests showed discrepancies between hydrate saturations derived from seismic methods [23,24]. This was probably because even in water-saturated environments, a notably small amount of residual gas can obscure the increase in velocity caused by the presence of hydrate. Therefore, we tried to obtain accurate quantification of methane hydrate saturation in combination with the ultrasonic velocity and attenuation.

At present, most reported apparatus used an embedded ultrasonic sensor to measure acoustic response of methane hydrate formation in bearing sediments [25–28]. However, in some special cases, such as the detection of the fidelity core on-board, an ultrasonic sensor cannot be embedded to realize the measurement of the pressure conserved cores. Therefore, it was necessary to design an external ultrasonic sensor apparatus for the detailed core analysis in the laboratory.

This study presented an ultrasonic test apparatus for pressure cores of natural methane hydrate-bearing sediments. This test system consisted of two main units, which can be used both for formation of hydrate at low temperature and non-embedded ultrasonic measurements at in situ pressures. The P-wave velocity and attenuation can then be combined to indicate hydrate saturation and morphology in the bearing sediments. This work provided a preliminary understanding of natural cores, which was significant for the subsequent exploration and detailed core analysis in a laboratory.

2. Materials and Methods

2.1. Apparatus and Materials

In this experimental apparatus, a special design of the chamber was performed according to the requirements of the in situ detection of the methane hydrate-bearing sediment, and the device structure was shown in Figure 1. The apparatus consisted of two main units: the hydrate formation unit and the ultrasonic test unit. The hydrate formation unit included a high pressure chamber that was packed with porous medium, a thermal control system, a pressure control system and a data acquisition system. To monitor the temperature of the system in real time, a high-sensitivity temperature sensor was used. To achieve the necessary experimental conditions at high pressures, a J-type thermistor was used in this system to monitor the temperature changes [29–32]. The main function of this unit was to generate the high-pressure and low-temperature conditions for the formation of hydrates.

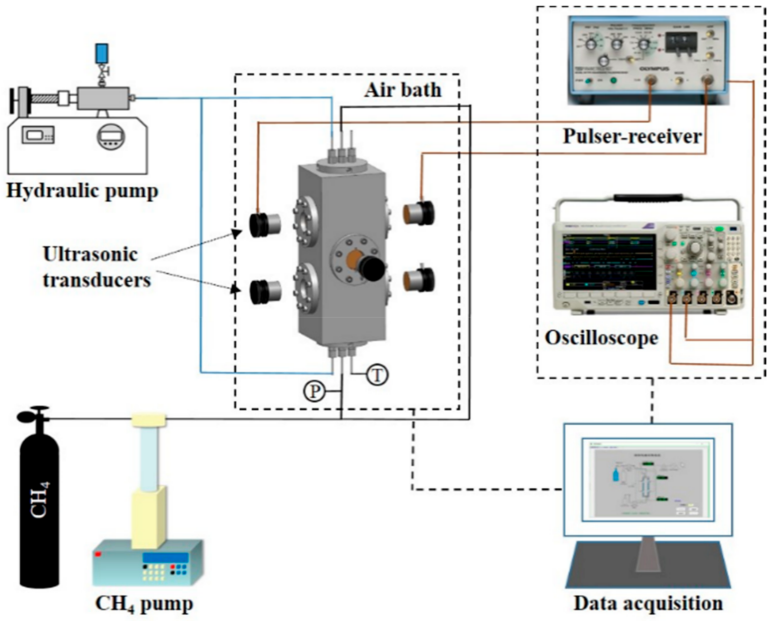

Figure 1. Diagram of the experimental apparatus.

The ultrasonic pulse receiver offered square wave excitation which was especially powerful in testing highly attenuated materials. Ultrasonic waves of different frequencies had different propagation characteristics in sediments. The ultrasonic signal had a strong resolution with high frequency and short wavelength, although the signal strength was easy to attenuate rapidly in the sediment sample. Therefore, it was of great significance to choose the appropriate ultrasonic frequency for measurement. To weigh the advantages and disadvantages, the frequency of the ultrasonic transducers used in the experiment was 100 kHz. The dynamic variation of the waveform was recorded by the computer for further analysis.

The ultrasonic transducers were fixed to the polymer protecting jackets which were designed to avoid wave diffraction and to withstand high pressure. Additionally, the protecting jackets also functioned as a matching layer, which increased the transmission through the pressure core between the transducers in terms of ultrasonic wave attenuation during propagation. Each polymer protecting jacket was embedded into a round hole with a diameter of 44 mm which penetrated through the sidewall of the chamber. The protecting jackets and the wall must be completely sealed to ensure the pressure stability in the chamber. The length and inner diameter of the chamber were 300 mm and 80 mm, respectively. The material and wall thickness were specially designed to withstand the high operating pressure up to 20 MPa. These parameters were considered to meet the requirements of on-board detection for pressure cores. The ultrasonic transducers used in the experiment can realize the switch between transmitting and receiving signals during the measurement process. A more comprehensive range of detection can be achieved to eliminate the non-detection zone.

To perform repeatable and reliable experiments, BZ-04 glass beads (As-One Co., Ltd., Osaka, Japan, 37.5% porosity) were densely packed into the high-pressure vessel in each separate case to investigate the effect on the ultrasonic characteristics of the hydrate saturation. To exclude the error caused by impurities, methane gas with high purity of 99.5% was obtained from Dalian DATE Special Gas Corporation (Dalian, China).

2.2. Experimental Procedures

Three pairs of ultrasonic transducers were symmetrically fixed using matched pressing cap and lock screws. To reduce energy attenuation, an ultrasonic couplant was smeared evenly on the surface of each ultrasonic transducer. All components were connected and debugged in advance. Clean and dry quartz sand was firstly packed into the vessel. The methane gas was injected to a

known pressure based on the hydrate content required. Then the hydrate was formed from liquid water by rapid cooling. In the water-rich method, secondary water injection was required in order to completely consume the methane gas. This would take approximately 500 min, which was regarded as the induction time before the formation of hydrate [33]. The driving force was mainly governed by CH_4 molecular diffusion. With sensors monitoring the pressure and temperature changes, when the pressure dropped sharply accompanied by the rise of temperature, the hydrate was considered to start to form. When the pressure and temperature are stabilized again for at least 2 h, the formation was considered completed. The waveforms of the methane hydrate-bearing sediment were displayed on a digital phosphor oscilloscope (DPO 4034B, Tektronix, Inc., Waltham, MA, USA) and the received signals were collected by the computer.

2.3. Theoretical Method

In this paper, the ultrasonic transmission method was used to measure the P-wave velocity of hydrate-bearing sediment, and three pairs of ultrasonic transducers were employed for transmitting and receiving ultrasonic signals. The transmission method required accurate measurements of the travel time of the ultrasonic waves and propagation distance through the sample. The P-wave velocity in the sample was determined by the travel times of the receiving signal since the sample size was fixed. The propagation distance L of the ultrasonic wave was the summation of the bearing sediment and the protecting layer. Therefore, the P-wave velocity of hydrate-bearing sediment was determined by Equation (1):

$$V_p = \frac{L}{t - t_0} = \frac{L}{t_p} \tag{1}$$

where L is the travel distance of the ultrasonic wave which is equal to the diameter of the pressure core in this paper, t is the measured travel time according to the first wave, t_0 is the system delay time which was directly measured in advance for calibration.

The spectral ratio method was one of the most widely used and stable algorithms for an inverse of attenuation (Q^{-1}) estimation [34,35]. Since the coda wave was easily disturbed by the inhomogeneous scattering, the direct wave was extracted in this paper to determine the attenuation of the waveform.

Briefly, the frequency content of the first cycle was analyzed by the fast Fourier transform. The amplitude spectrum of the sample was divided by that of the standard aluminum sample in the same geometry. The P-wave attenuation (Q^{-1}) is expressed using the inverse of the quality factor Q which is calculated by:

$$Q = \frac{\pi L}{\gamma V_p} \tag{2}$$

where the dimensionless Q is the quality factor, L is the length of the samples, V_p is the measured velocity, and γ is the slope of the frequency ratios which can be calculated by:

$$\mathrm{In}\left(\frac{A_1}{A_2}\right) = \gamma L f + \mathrm{In}\left(\frac{G_1}{G_2}\right) \tag{3}$$

where A_1 and A_2 are the amplitudes of the standard sample and test sample waveform at the same frequency, respectively. f is the frequency, G_1 and G_2 are the geometric diffusion factors which generally only depend on the detection distance.

Through quantitative water mixed with the sands in advance, excessive methane gas was then injected to convert water into hydrate completely. The pore space would be filled with hydrate and residual methane gas after the formation of hydrate. This method is called excess gas method in which the final hydrate saturation is controlled by the initial water content. The content of hydrate increases with the initial water saturation S_w. The hydrate saturation generated by the excess gas method is calculated by Equation (4):

$$S_h = \frac{m_w M_H}{N_H M_W \rho_H V_{pore}} \tag{4}$$

where, N_H represents the hydration number of hydrate (in this paper, the value was 6), m_w is the mass of deionized water (assuming that 100% deionized water is converted to hydrate), M_H and M_W are the molar masses of hydrate and water, respectively, ρ_H is the density of hydrate, and V_{pore} represents the pore volume of the bearing sediment. The experimental conditions are shown in Table 1. The feasibility and calibration tests have already been conducted in our previous paper [29] to verify the performance.

Table 1. Summary of experimental initial conditions, peak frequencies, slope of the frequency ratios, attenuation and calculated velocities for excess gas cases.

Case	m_w (g)	S_h (%)	f_p (Hz)	γ ($\times 10^{-4}$)	Q^{-1}	V_P (m/s)
Standard	-	-	195,843	-	-	6320
Blank	0	0	42,684 ± 116	2.54 ± 0.15	1.007 ± 0.005	1793 ± 15
1	7	2	43,562 ± 189	3.04 ± 0.20	1.326 ± 0.010	2023 ± 11
2	28	8	42,090 ± 223	3.15 ± 0.26	1.488 ± 0.018	2183 ± 33
3	53	15	39,738 ± 158	3.30 ± 0.24	1.464 ± 0.028	2277 ± 27
4	70	20	39,596 ± 175	3.34 ± 0.26	1.636 ± 0.020	2477 ± 19
5	105	30	42,399 ± 195	3.55 ± 0.28	1.863 ± 0.040	2552 ± 44
6	140	40	43,111 ± 145	3.76 ± 0.36	2.210 ± 0.017	2836 ± 32
7	175	50	42,090 ± 197	4.00 ± 0.45	2.241 ± 0.023	3047 ± 42
8	210	60	42,826 ± 134	4.25 ± 0.54	2.603 ± 0.036	3114 ± 53

The experimental initial conditions of the excess gas method are shown in Table 1. In these cases, the air bath was preset to 274 K for cooling down. Meanwhile, the data acquisition system collected the temperature and pressure signal every 10 s automatically while the ultrasonic signal was manually collected.

To explore the influence of formation methodologies on the ultrasonic properties of hydrate sediments, we further conducted a series of excessive water generating experiments. The ISCO pump was used to inject a certain amount of methane gas into the chamber to reach a preset value. The pressure and temperature values were recorded simultaneously, and the gas amount injected would eventually control the saturation of the hydrate. The calculated method can be expressed by Equation (5):

$$S_h = \frac{nM_H}{\rho_H V_{pore}} \tag{5}$$

where, M_H represents the molar mass of hydrate, ρ_H is the density of hydrate, V_{pore} is the pore volume of sediment. n represents the total moles of methane gas injected into the system which could be determined by the P-R equation of state. By controlling the initial gas injection pressure, 8 samples with hydrate saturation ranging from 4% to 40% were obtained, and P-wave detection was performed for each sediment sample. The experimental conditions were listed in Table 2.

Table 2. Summary of experimental initial conditions, peak frequencies, slope of the frequency ratios, attenuation and calculated velocities for excess water cases.

Case	n (mol)	S_h (%)	f_p (Hz)	γ ($\times 10^{-4}$)	Q^{-1}	V_P (m/s)
Standard	-	-	195,843	-	-	6320
Blank	0	0	75,801 ± 116	1.40 ± 0.13	1.811 ± 0.015	1807 ± 9
9	0.130	4	69,982 ± 189	1.84 ± 0.20	2.446 ± 0.013	1813 ± 13
10	0.259	8	66,508 ± 223	2.01 ± 0.21	2.737 ± 0.041	1857 ± 23
11	0.324	10	69,804 ± 158	1.95 ± 0.26	2.991 ± 0.035	1886 ± 36
12	0.486	15	67,785 ± 175	2.11 ± 0.28	3.291 ± 0.025	1945 ± 24
13	0.648	20	63,747 ± 195	2.18 ± 0.25	3.607 ± 0.062	2152 ± 46
14	0.810	25	66,865 ± 145	2.35 ± 0.35	4.248 ± 0.048	2362 ± 18
15	0.972	30	65,558 ± 197	2.26 ± 0.30	4.852 ± 0.067	2488 ± 25
16	1.296	40	63,569 ± 134	2.45 ± 0.34	5.269 ± 0.090	2669 ± 37

2.4. Calibration Test

We measured several different sized polymer protecting jackets to test the accuracy of our measurements as shown in Figure 2. The slope of the length over travel time is the velocity of the measured material. Similarly, the velocity for standard aluminium sample was also measured within a 0.9% deviation compared to Pohl's paper [25]. In this system, the ultrasonic transducer was not directly in contact with the pressure core sample. Therefore, it was necessary to measure the system delay before calculating P-wave velocity. The delay time was related to the internal structure of the transducers which can be read from the oscilloscope directly by connecting the transmitter and receiver connected with two protecting jackets. Every excess water sample was pretested for porosity by the water injection method. We assumed that the porosity did not change throughout each experiment.



Figure 2. Polymer protecting jackets with different diameters.

3. Results and Discussion

3.1. Effects of the Excess Gas Method on P-Wave Variation

Figure 3 shows the changes of the waveform, temperature and pressure signals over time during the formation of methane hydrate for Case 6. Before the formation of hydrate, the waveform was affected by the gas in pores when penetrating the sediments, resulting in severe attenuation.

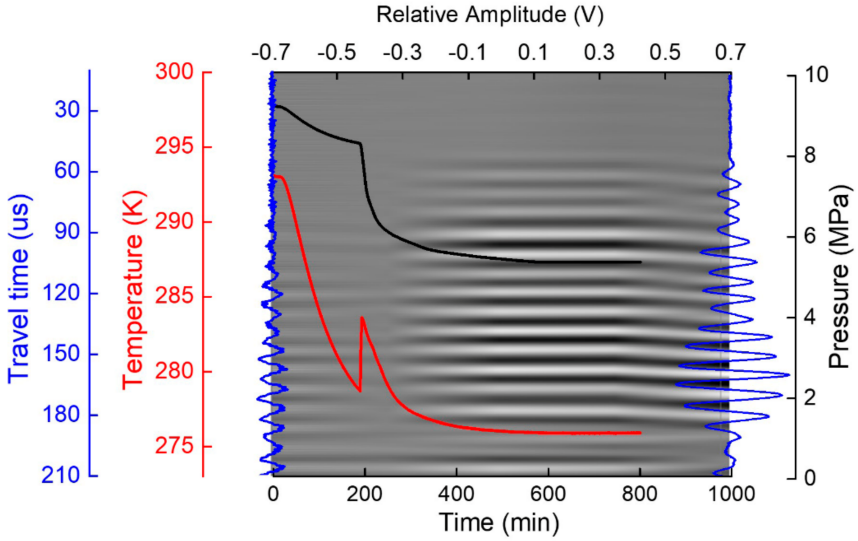

Figure 3. Changes of the waveform, temperature and pressure signals over time during the formation and dissociation of methane hydrate using the excess gas method.

The relative amplitude for the received signal was less than 0.10 V when the vibrations were fully developed. At approximately 220 min, the hydrate began to form, which can be determined from the

temperature and pressure curve. However, at this time, the P-wave velocity and amplitude of sediments were basically unchanged. Then, within the time range of 300 min to 500 min, the downward trend of the pressure curve indicated that the hydrate continued to form. In this time period, the corresponding ultrasonic signal experienced a mutation, mainly reflected in the relative amplitude for the received signal increasing to 0.31 V with an increment of 210% compared to the hydrate-free state. This phenomenon indicated that the presence of hydrate could significantly change the elastic properties of the sediments, which might indicate that the change of P-wave velocity and amplitude mainly occurred at the late stages of hydrate formation.

After 700 min, the pressure and the travel time of the first wave remained constant, it could be considered that the hydrate formation process was largely finished and that the system had reached an equilibrium state. Figure 4 showed the direct waveform data of the pressure cores with different hydrate saturation under the condition of excessive gas. Different initial water saturations resulted in different amplitudes of the signals before hydrate formation. Under the conditions of the excess gas method, water would be completely transformed into hydrate. Attenuation of amplitude was especially important since P-velocity was not sensitive in high gas saturation regime.

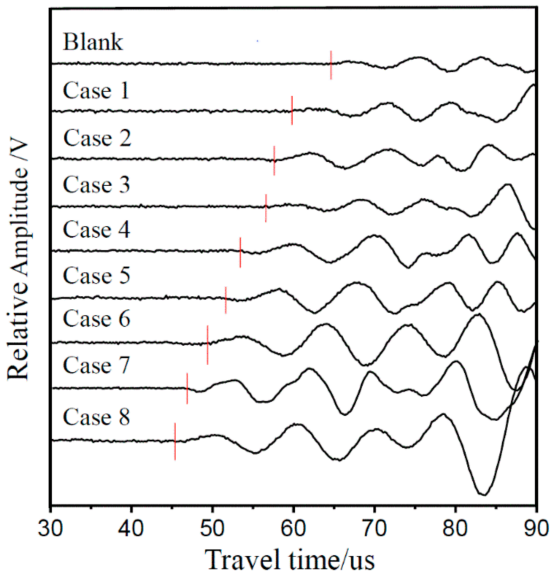

Figure 4. Signal waveform of hydrate-bearing sediment samples with different hydrate saturations in the excess gas method.

As the hydrate saturation increased gradually, the penetrating efficiency of P-waves increased gradually which appeared as an increase of amplitude. By comparing the waveforms of different initial water saturation samples, the travel times started to show different tendencies. On the whole, the changes of wave velocity and amplitude depended on the range of hydrate saturation. In the low saturation range 0% to 8%, the wave velocity increased significantly with saturation showing that an 8% rise in the hydrate saturation caused the velocity to change from 1793 m/s to 2183 m/s as depicted in Table 1. Correspondingly, in the high saturation scope 50% to 60%, the further increase in the saturation caused the increase of P-wave amplitude but the velocity remained relative stable. It showed that a 10% increase in hydrate saturation made the velocity change from 3047 m/s to 3114 m/s with an order of magnitude lower than before. Different from the wave velocity, the amplitude maintained a gentle increasing trend for hydrate saturation even up to 60%. Therefore, we believed that in the excess gas method, the amplitude would better reflect the change of hydrate saturation than the P-wave velocity. The attenuation estimation will be elaborated on later.

3.2. *Effects of the Excess Water Method on P-Wave Variation*

Figure 5 showed the changes of the waveform, temperature and pressure signals during the formation of methane hydrate for Case 14. Different from the method of excess gas formation, the pore space was dominated by liquid phase before hydrate formation, and methane gas mainly existed in the form of gas bubbles. The acoustic waves had less attenuation when penetrating sediments compared with high gas saturation cases. The relative amplitude could reach 0.37 V, which was more than three times of the vibrations in excess gas method. After the formation of the hydrate, the gas pressure decreased rapidly from 9.2 MPa to 8.7 MPa. The continuous consumption of gas and free water in the pores led to the approach of the phase state to the equilibrium line. The reduction of the driving force was insufficient to convert methane gas into hydrate completely. Therefore, secondary water injection was required to increase the pressure until the gas was entirely converted into hydrate. Due to the continuous formation of hydrate, the component in the pores changed from initial gas-liquid two phases to gas-liquid-solid three phases. The change of pore components impeded the transmission of acoustic energy. Thus, after the hydrate started to form, the acoustic amplitude decreased from 0.37 V to 0.18 V. After 2000 min, the temperature, pressure and waveform were largely unchanged. The hydrate formation process could be considered as finished, and the hydrate saturation reached its maximum which was determined by the initial gas saturation.

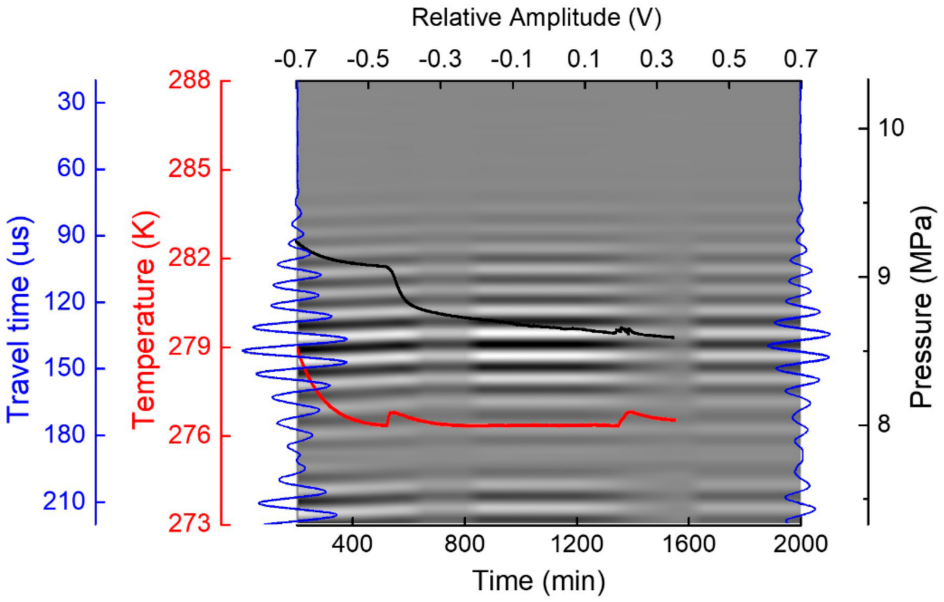

Figure 5. Changes of the waveform, temperature and pressure signals over time during the formation of methane hydrate in the water-rich method.

Figure 6 shows the waveform diagram of the sediment samples with different hydrate saturations under the condition of excess water. In the low saturation range of 0% to 15%, the P-wave velocity did not increase significantly when compared with the excess gas method. As shown in Table 2, a 15% increase in hydrate saturation caused the velocity to change from 1807 m/s to 1945 m/s. When the saturation reached 15% to 30%, the overall ultrasonic and mechanical properties of the sediment began to change significantly, showing that the same increase in hydrate saturation made the velocity change from 1945 m/s to 2488 m/s. When the saturation further increased, the P-wave velocity did not change significantly.

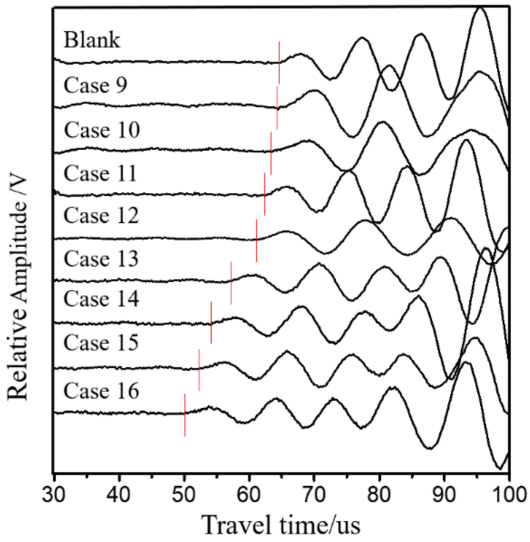

Figure 6. Signal waveform of hydrate-bearing sediment samples with different hydrate saturations in the excess water method.

3.3. Effects of Hydrate Saturation on Attenuation

Figure 7a c showed the frequency spectra for the hydrate-bearing sediment samples with different saturations calculated from the first cycle of the direct wave. The aluminium standard sample, plotted with a dashed line, had a peak frequency of more than 195 kHz, which was much higher than the other samples. As shown in the fourth column of Table 1, for the excess gas hydrate samples, the main frequency of all cases, including the hydrate-free and hydrate-containing samples, was located approximately 41 ± 3 kHz, indicating that the formation of hydrate did not change the location of the main frequency.

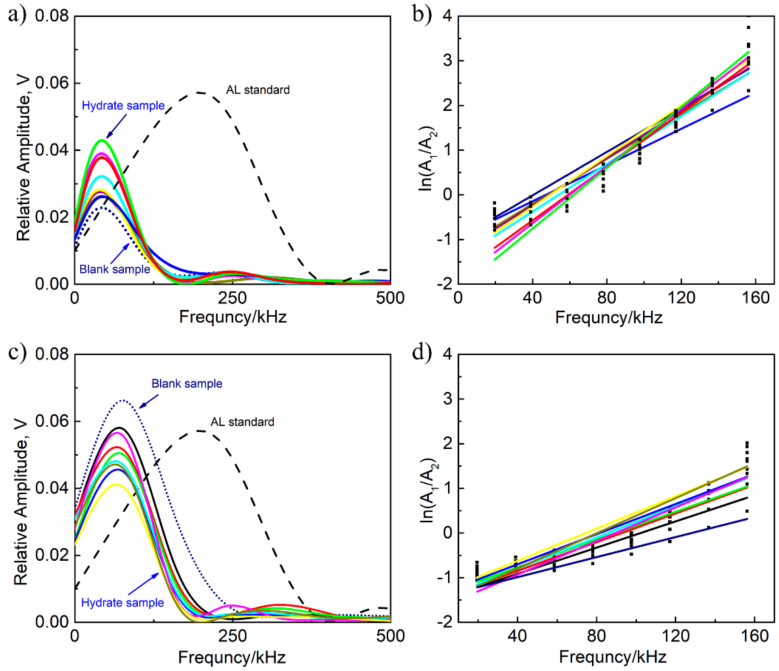

Figure 7. Comparison of the frequency spectra for excess gas (**a**) and water (**b**) method samples. Linear fitting of spectral ratios for excess gas (**c**) and water (**d**) cases. The colours of the fitting lines in (**b**) and (**d**) corresponded to the spectra in (**a**) and (**c**), respectively.

Visibly different from the main frequency distribution, as seen in Figure 7a, the gradient of the spectral intensity is related to hydrate saturation. When the gas saturation in the pressure core is high, and the waveform attenuation is so serious that the arrival time of the first wave cannot be directly distinguished, the hydrate saturation can be approximately estimated using this method. However, this method was also limited by the formation methodology. To investigate the effects, the excess water cases were also calculated with the results depicted in Figure 7c. We found that the hydrate saturation had just the opposite effect on the spectral intensity. We inferred that the contradiction was mainly caused by the discrepancies of the original time-domain spectrogram as shown in Figures 4 and 6. Furthermore, as seen from Table 2, the main frequency of the hydrate-free sample was located approximately 76 kHz which was higher than that of the hydrate-bearing cores, which were mostly between 63 kHz and 70 kHz, indicating that the formation of hydrate caused the frequency spectrum to shift towards a lower frequency. Furthermore, the gradient of displacement is closely related to the hydrate saturation. Compared with the hydrate-free sample, when the hydrate saturation is in the range of 4% to 40%, the corresponding frequency content decreased by approximately 8% to 16%.

According to Toksöz's method [34], the spectrum ratio was fitted in the main frequency range of the direct wave. Therefore, the longitudinal spectral ratio frequency band in this study was selected between 20 kHz and 150 kHz. It was reasonable to think that this range is justified and accurate since all peaks for the cases were located in this frequency band, as shown in Figure 7a c. The data points were obtained by comparing the amplitude ratios of the hydrate and standard samples at the same frequency. The slopes of the frequency ratios were depicted in Figure 7b,d by linear fitting the data points. The colour of the fitting line corresponded to the frequency spectra in Figure 7a c. The slope obtained by fitting was proportional to γ in Equation (3). We then calculated the P-wave attenuation (Q^{-1}) using Equation (2), and the results were shown in Tables 1 and 2. Experimental errors for the attenuation calculations were evaluated for each variable in Equation (2) and were also presented. The maximum relative error was less than 2.2% which was reasonable and within the margin of acceptable uncertainties.

To quantify the relationship between ultrasonic attenuation and hydrate saturation, the experimental results were plotted in Figure 8 together with error bars. The error bars indicated the confidence in each measurement and the uncertainty in calculation for each case. Different from the variation law of wave velocity, especially for excess water cases, there existed a liner relationship between the P-wave attenuation (Q^{-1}) and hydrate saturation within the range of hydrate saturation covered by all of the experimental cases. According to the fitting results in Figure 8b, R^2 can reach 97% when the variation of error was considered. For the excess gas cases, when the hydrate saturation was lower than 20%, the relation between the attenuation coefficient and the saturation change is closer to the logarithmic regulation. When the hydrate saturation is higher than 20%, the relation of attenuation coefficient with the change of saturation turned to linear and the R^2 value can reach 99% after piecewise fitting which was shown in Figure 8a.

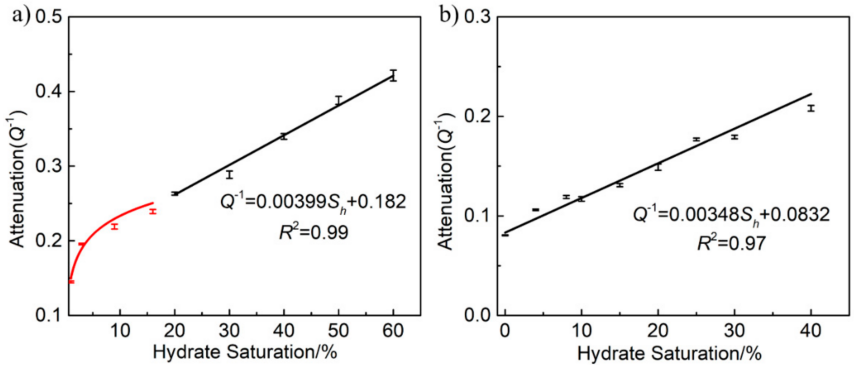

Figure 8. Relation between attenuation (Q^{-1}) and hydrate saturation in consideration of experimental errors: (**a**) excess-gas and (**b**) excess-water.

3.4. Effects of Hydrate Saturation on P-Wave Velocity

The P-wave response is an important characteristic which can give information about the occurrence and evolution of methane gas hydrate in porous sediments. Such knowledge could be used to infer the saturation of hydrate if the relationship between them was known [36–40]. Several elastic velocity models had been developed to predict this relationship [41–44]. Figure 9 showed that the P-wave velocity changed with the hydrate saturation using the excess-gas (a) and excess-water (b) methodology. Furthermore, in order to analyse the occurrence patterns of hydrate in porous sediments, the P-wave velocity curve predicted by the effective medium model [45] was also introduced in the figure for validation. To objectively compare the approaches described, we required a consistent set of input parameters. The physical constants were shown in Table 3.

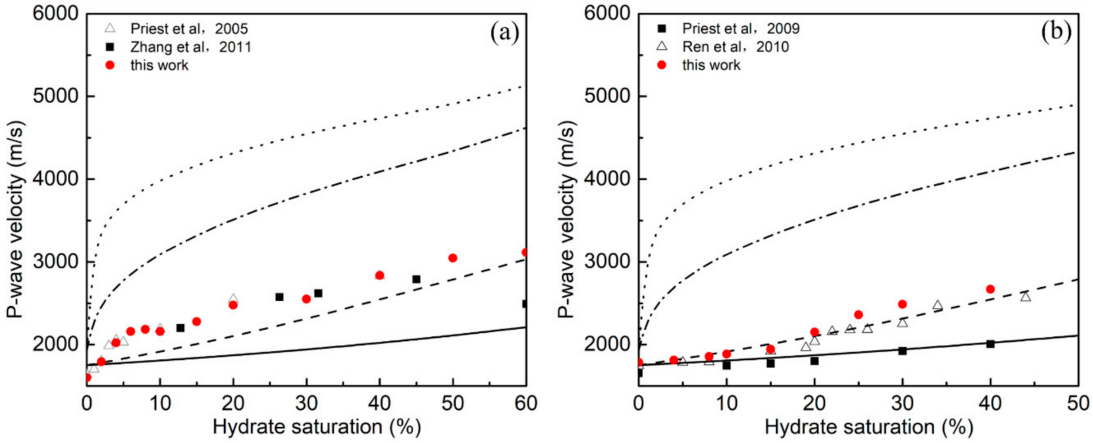

Figure 9. Relation between P-wave velocity and hydrate saturation compared with models. (**a**) excess-gas and (**b**) excess-water.

Table 3. Model parameters for P-wave velocity predictions.

Parameter	Value
Critical porosity	0.35
Quartz bulk modulus	36 GPa
Quartz shear modulus	45 GPa
Quartz density	2580 kg m^{-3}
Hydrate bulk modulus	7.7 GPa
Hydrate shear modulus	3.2 GPa
Hydrate density	910 kg m^{-3}
Water bulk modulus	2.3 GPa
Water density	1030 kg m^{-3}
Gas bulk modulus	0.1 GPa
Gas density	230 kg m^{-3}
Viscosity of water	2.04×10^{-3} Pa s
Viscosity of gas	1.34×10^{-3} Pa s

Different methodologies for forming hydrate can result in different velocity tendencies. The processes of hydrate nucleation and growth governed the hydrate occurrence. The modeling results plotted using dotted lines in Figure 9 were from Dai's paper [46], which represented the wave velocities for hydrate forming as cement at grain contacts. The wave velocity significantly increased for low hydrate saturations and became stable gradually. The red data points in Figure 9a showed the P-wave velocities measured in the excess-gas samples which correlated well with the hydrate saturation and was largely reproduced by the prediction of this fitting line. Specifically, the velocity increased from 1793 m/s to 2277 m/s in the saturation range of 0% to 15%, with a change scale of 27.0%, even greater than the range of 20% to 60% with an increase of 25.7%. Comparing the measured P-wave

velocity with the research of Priest et al. [41] and Zhang et al. [42], it was found that the general velocity trend of hydrate sediments generated in the excess gas method was similar.

Other types of hydrate occurrence were also plotted in Figure 9. Dot-dashed curves predicted the wave velocities for grain cementing hydrate [47], dashed curves showed the load bearing hydrate [48], and solid curves presented the pore filling hydrate [49]. The P-wave velocity measured by the excess water methodology was scattered in Figure 9b, the experimental results was generally close to the dashed line with the P-wave velocity increasing steadily. There was no sudden increase of the excess gas samples when the saturation was less than 10%. The measured P-wave velocity presented a trend towards the development of the load-bearing curve. We compared the measured P-wave velocity with the research of Ren et al. [44], it was found that the overall trends by the excess water method in sandy sediments were similar. In the measured saturation scale, the P-wave velocity also correlated well with the experimental results of Ren et al. It can be predicted that hydrate with load-bearing distributions was often concentrated in the water-rich seabed stratum.

4. Conclusions

A method was developed to obtain the ultrasonic characteristics of pressure cores at in situ pressures. By controlling the gas and water content, we obtained 16 samples using different methodologies with hydrate saturations ranging from 2% to 60%. The P-wave detection was performed in situ for each separate sample.

The spectrum ratio method was applied in the main frequency band of the direct wave. The first cycle of the waveforms was analysed for its frequency content using a Fast Fourier transformation. Through linear fitting of the attenuation (Q^{-1}) to the hydrate saturation, the average deviation R^2 can reach more than 97%. Particularly for the excess water samples, two relationships were obtained using logarithmic and linear fitting methods, respectively. The hydrate saturation can be successfully predicted by the gradient of spectral intensity. This approach provided a new method for the acoustic measurement of the hydrate saturation when the arrival time of the first wave cannot be directly distinguished.

To obtain the relation between the P-wave velocity and hydrate saturation under various formation conditions, the velocity curve predicted by the effective medium model was introduced for validation. Our results demonstrated that both the velocity and attenuation were sensitive to hydrate saturation. We think that the specially designed non-embedded ultrasonic detection apparatus could assist hydrate resource exploration and detailed core analysis.

Author Contributions: Conceptualization, J.Z. and X.L.; Methodology, J.Z. and Y.L.; Validation, L.Y.; Writing-Original Draft Preparation, X.L.; Supervision, H.Z., B.X., X.L., H.Y., W.P., Q.L. and Y.S.

Funding: This study has been supported by the National Key R&D Program of China (2017YFC0307300), the Major Program of National Natural Science Foundation of China (Grant No. 51436003) and the National Natural Science Foundation of China (Grant No. 51227005, Grant No. 51376034 and Grant No. 51276028).

Acknowledgments: The authors acknowledge the National Key R&D Program of China (2017YFC0307300), the Major Program of National Natural Science Foundation of China (Grant No. 51436003) and the National Natural Science Foundation of China (Grant No. 51227005, Grant No. 51376034 and Grant No. 51276028).

Conflicts of Interest: The authors declare no conflict of interest.

References

1. Sloan, E.D., Jr. Fundamental principles and applications of natural gas hydrates. *Nature* **2003**, *426*, 353. [CrossRef] [PubMed]
2. Walsh, M.R.; Koh, C.A.; Sloan, E.D.; Sum, A.K.; Wu, D.T. Microsecond simulations of spontaneous methane hydrate nucleation and growth. *Science* **2009**, *326*, 1095–1098. [CrossRef]
3. Christiansen, R.L.; Sloan, E.D., Jr. Mechanisms and kinetics of hydrate formation. *Annal. N. Y. Acad. Sci.* **1994**, *715*, 283–305. [CrossRef]

4. Yang, L.; Falenty, A.; Chaouachi, M.; Haberthür, D.; Kuhs, W.F. Synchrotron X-ray computed microtomography study on gas hydrate decomposition in a sedimentary matrix. *Geochem. Geophys. Geosyst.* **2016**, *17*, 3717–3732. [CrossRef]
5. Zhao, J.; Cheng, C.; Song, Y.; Liu, W.; Liu, Y.; Xue, K.; Zhu, Z.; Yang, Z.; Wang, D.; Yang, M. Heat transfer analysis of methane hydrate sediment dissociation in a closed reactor by a thermal method. *Energies* **2012**, *5*, 1292–1308. [CrossRef]
6. Song, Y.; Zhang, L.; Lv, Q.; Yang, M.; Ling, Z.; Zhao, J. Assessment of gas production from natural gas hydrate using depressurization, thermal stimulation and combined methods. *RSC Adv.* **2016**, *6*, 47357–47367. [CrossRef]
7. Zhao, J.; Song, Y.; Lim, X.L.; Lam, W.H. Opportunities and challenges of gas hydrate policies with consideration of environmental impacts. *Renew. Sustain. Energy Rev.* **2017**, *70*, 875–885. [CrossRef]
8. Zhang, L.; Yang, L.; Wang, J.; Zhao, J.; Dong, H.; Yang, M.; Liu, Y.; Song, Y. Enhanced CH_4 recovery and CO_2 storage via thermal stimulation in the CH_4/CO_2 replacement of methane hydrate. *Chem. Eng. J.* **2017**, *308*, 40–49. [CrossRef]
9. Wang, B.; Huo, P.; Luo, T.; Fan, Z.; Liu, F.; Xiao, B.; Yang, M.; Zhao, J.; Song, Y. Analysis of the physical properties of hydrate sediments recovered from the pearl river mouth basin in the South China Sea: Preliminary investigation for gas hydrate exploitation. *Energies* **2017**, *10*, 531. [CrossRef]
10. Liang, Y.; Liu, S.; Wan, Q.; Li, B.; Liu, H.; Han, X. Comparison and optimization of methane hydrate production process using different methods in a single vertical well. *Energies* **2019**, *12*, 124. [CrossRef]
11. Yang, L.; Zhao, J.; Liu, W.; Li, Y.; Yang, M.; Song, Y. Microstructure observations of natural gas hydrate occurrence in porous media using microfocus x-ray computed tomography. *Energy Fuels* **2015**, *29*, 4835–4841. [CrossRef]
12. Zhao, J.; Wang, B.; Sum, A.K. Dynamics of hydrate formation and deposition under pseudo multiphase flow. *AIChE J.* **2017**, *63*, 4136–4146. [CrossRef]
13. Wang, S.; Yang, M.; Wang, P.; Zhao, Y.; Song, Y. In situ observation of methane hydrate dissociation under different backpressures. *Energy Fuels* **2015**, *29*, 3251–3256. [CrossRef]
14. Castagna, J.P.; Batzle, M.L.; Eastwood, R.L. Relationships between compressional-wave and shear-wave velocities in clastic silicate rocks. *Geophysics* **1985**, *50*, 571–581. [CrossRef]
15. Winters, W.J.; Waite, W.F.; Mason, D.H.; Gilbert, L.Y.; Pecher, I.A. Methane gas hydrate effect on sediment acoustic and strength properties. *J. Pet. Sci. Eng.* **2007**, *56*, 127–135. [CrossRef]
16. Yang, J.; Tohidi, B. Determination of hydrate inhibitor concentrations by measuring electrical conductivity and acoustic velocity. *Energy Fuels* **2013**, *27*, 736–742. [CrossRef]
17. Chand, S.; Minshull, T.A.; Gei, D.; Carcione, J.M. Elastic velocity models for gas-hydrate-bearing sediments—A comparison. *Geophys. J. Int.* **2004**, *159*, 573–590. [CrossRef]
18. Konno, Y.; Jin, Y.; Yoneda, J.; Kida, M.; Egawa, K.; Ito, T.; Suzuki, K.; Nagao, J. Effect of methane hydrate morphology on compressional wave velocity of sandy sediments: Analysis of pressure cores obtained in the Eastern Nankai Trough. *Mar. Pet. Geol.* **2015**, *66*, 425–433. [CrossRef]
19. Waite, W.F.; Winters, W.J.; Mason, D.H. Methane hydrate formation in partially water-saturated Ottawa sand. *Am. Min.* **2004**, *89*, 1202–1207. [CrossRef]
20. Yun, T.S.; Francisca, F.M.; Santamarina, J.C.; Ruppel, C. Compressional and shear wave velocities in uncemented sediment containing gas hydrate. *Geophys. Res. Lett.* **2005**, *32*. [CrossRef]
21. Lee, J.Y.; Francisca, F.M.; Santamarina, J.C.; Ruppel, C. Parametric study of the physical properties of hydrate-bearing sand, silt, and clay sediments: 2. Small-strain mechanical properties. *J. Geophys. Res. Solid Earth* **2010**, *115*. [CrossRef]
22. Winters, W.J.; Pecher, I.A.; Waite, W.F.; Mason, D.H. Physical properties and rock physics models of sediment containing natural and laboratory-formed methane gas hydrate. *Am. Mineral.* **2004**, *89*, 1221–1227. [CrossRef]
23. Sahoo, S.K.; Marín-Moreno, H.; North, L.J.; Falcon-Suarez, I.; Madhusudhan, B.N.; Best, A.I.; Minshull, T.A. Presence and consequences of co-existing methane gas with hydrate under two phase water-hydrate stability conditions. *J. Geophys. Res. Solid Earth* **2018**, *123*, 3377–3390. [CrossRef]
24. Sahoo, S.K.; Madhusudhan, B.N.; Marín-Moreno, H.; North, L.J.; Ahmed, S.; Falcon-Suarez, I.H.; Minshull, T.A.; Best, A.I. Laboratory Insights into the Effect of Sediment-Hosted Methane Hydrate Morphology on Elastic Wave Velocity from Time-Lapse 4-D Synchrotron X-Ray Computed Tomography. *Geochem. Geophys. Geosyst.* **2018**, *19*, 4502–4521. [CrossRef]
25. Pohl, M.; Prasad, M.; Batzle, M.L. Ultrasonic attenuation of pure tetrahydrofuran hydrate. *Geophys. Prospect.* **2018**, *66*, 1349–1357. [CrossRef]

26. Helgerud, M.B.; Waite, W.F.; Kirby, S.H.; Nur, A. Elastic wave speeds and moduli in polycrystalline ice Ih, sI methane hydrate, and sII methane-ethane hydrate. *J. Geophys. Res. Solid Earth* **2009**, *114*. [CrossRef]
27. Hu, G.; Ye, Y.; Zhang, J.; Liu, C.; Diao, S.; Wang, J. Acoustic properties of gas hydrate-bearing consolidated sediments and experimental testing of elastic velocity models. *J. Geophys. Res. Solid Earth* **2010**, *115*, B2. [CrossRef]
28. Bu, Q.; Hu, G.; Ye, Y.; Liu, C.; Li, C.; Wang, J. Experimental study on 2-D acoustic characteristics and hydrate distribution in sand. *Geophys. J. Int.* **2017**, *211*, 990–1004. [CrossRef]
29. Yang, L.; Zhou, W.; Xue, K.; Wei, R.; Ling, Z. A pressure core ultrasonic test system for on-board analysis of gas hydrate-bearing sediments under in situ pressures. *Rev. Sci. Instrum.* **2018**, *89*, 054904. [CrossRef]
30. Song, Y.; Kuang, Y.; Fan, Z.; Zhao, Y.; Zhao, J. Influence of core scale permeability on gas production from methane hydrate by thermal stimulation. *Int. J. Heat Mass Transf.* **2018**, *121*, 207–214. [CrossRef]
31. Kuang, Y.; Lei, X.; Yang, L.; Zhao, Y.; Zhao, J. Observation of in-situ growth and decomposition of Carbon dioxide hydrate at gas-water interfaces using MRI. *Energy Fuels* **2018**, *32*, 6964–6969. [CrossRef]
32. Zhao, J.; Zhang, L.; Chen, X.; Zhang, Y.; Liu, Y.; Song, Y. Combined replacement and depressurization methane hydrate recovery method. *Energy Explor. Exploit.* **2016**, *34*, 129–139. [CrossRef]
33. Natarajan, V.; Bishnoi, P.R.; Kalogerakis, N. Induction phenomena in gas hydrate nucleation. *Chem. Eng. Sci.* **1994**, *49*, 2075–2087. [CrossRef]
34. Toksöz, M.N.; Johnston, D.H.; Timur, A. Attenuation of seismic waves in dry and saturated rocks: 1. Laboratory measurement. *Geophysics* **1979**, *44*, 681–690. [CrossRef]
35. Johnston, D.H.; Toksöz, M.N.; Timur, A. Attenuation of seismic waves in dry and saturated rocks: II. Mechanisms. *Geophysics* **1979**, *44*, 691–711. [CrossRef]
36. Jakobsen, M.; Hudson, J.A.; Minshull, T.A.; Singh, S.C. Elastic properties of hydrate-bearing sediments using effective-medium theory. *J. Geophys. Res. Solid Earth* **2000**, *105*, 561–577. [CrossRef]
37. Gei, D.; Carcione, J.M. Acoustic properties of sediments saturated with gas hydrate, free gas and water. *Geophys. Prospect.* **2003**, *51*, 141–158. [CrossRef]
38. Carcione, J.M.; Tinivella, U. Bottom-simulating reflectors: Seismic velocities and AVO effects. *Geophysics* **2000**, *65*, 54–67. [CrossRef]
39. Ecker, C.; Dvorkin, J.; Nur, A.M. Estimating the amount of gas hydrate and free gas from marine seismic data. *Geophysics* **2000**, *65*, 565–573. [CrossRef]
40. Lee, M.W.; Hutchinson, D.R.; Collett, T.S.; Dillon, W.P. Seismic velocities for hydrate-bearing sediments using weighted equation. *J. Geophys. Res. Solid Earth* **1996**, *101*, 20347–20358. [CrossRef]
41. Priest, J.A.; Best, A.I.; Clayton, C.R.I. A laboratory investigation into the seismic velocities of methane gas hydrate-bearing sand. *J. Geophys. Res. Solid Earth* **2005**, *110*. [CrossRef]
42. Zhang, Q.; Li, F.; Sun, C.; Li, Q.; Wu, X.; Liu, B.; Chen, G. Compressional wave velocity measurements through sandy sediments containing methane hydrate. *Am. Mineral.* **2011**, *96*, 1425–1432. [CrossRef]
43. Priest, J.A.; Rees, E.V.L.; Clayton, C.R.I. Influence of gas hydrate morphology on the seismic velocities of sands. *J. Geophys. Res. Solid Earth* **2009**, *114*. [CrossRef]
44. Ren, S.; Liu, Y.; Liu, Y.; Zhang, W. Acoustic velocity and electrical resistance of hydrate bearing sediments. *J. Pet. Sci. Eng.* **2010**, *70*, 52–56. [CrossRef]
45. Ecker, C.; Dvorkin, J.; Nur, A.M. Sediments with gas hydrates: Internal structure from seismic AVO. *Geophysics* **1998**, *63*, 1659–1669. [CrossRef]
46. Kleinberg, R.L.; Dai, J. Estimation of the mechanical properties of natural gas hydrate deposits from petrophysical measurements. In Proceedings of the Offshore Technology Conference, Houston, TX, USA, 2–5 May 2005.
47. Guerin, G.; Goldberg, D.; Meltser, A. Characterization of in situ elastic properties of gas hydrate-bearing sediments on the Blake Ridge. *J. Geophys. Res. Solid Earth* **1999**, *104*, 17781–17795. [CrossRef]
48. Helgerud, M.B.; Dvorkin, J.; Nur, A.; Sakai, A.; Collett, T. Elastic-wave velocity in marine sediments with gas hydrates: Effective medium modeling. *Geophys. Res. Lett.* **1999**, *26*, 2021–2024. [CrossRef]
49. Murray, D.R.; Fukuhara, M.; Osawa, O.; Endo, T.; Kleinberg, R.L.; Sinha, B.K.; Namikawa, T. Saturation, acoustic properties, growth habit, and state of stress of a gas hydrate reservoir from well logs. *Petrophysics* **2006**, *47*, 129–137.



© 2019 by the authors. Licensee MDPI, Basel, Switzerland. This article is an open access article distributed under the terms and conditions of the Creative Commons Attribution (CC BY) license (http://creativecommons.org/licenses/by/4.0/).